

# Machine learning of the Ising model on a spherical Fibonacci lattice

Zheng Zhou,<sup>1</sup> Chen-Hui Song,<sup>2</sup> Xu-Yang Hou,<sup>1,\*</sup> and Hao Guo<sup>1,3,†</sup>

<sup>1</sup>*School of Physics, Southeast University, Jiulonghu Campus, Nanjing 211189, China*

<sup>2</sup>*Tsinghua Shenzhen International Graduate School, Tsinghua University, Shenzhen 518055, China*

<sup>3</sup>*Hefei National Laboratory, Hefei 230088, China*

We investigate the Ising model on a spherical surface, utilizing a Fibonacci lattice to approximate uniform coverage. This setup poses challenges in achieving consistent lattice distribution across the sphere for comparison with planar models. We employ Monte Carlo simulations and graph convolutional networks (GCNs) to study spin configurations across a range of temperatures and to determine phase transition temperatures. The Fibonacci lattice, despite its uniformity, contains irregular sites that influence spin behavior. In the ferromagnetic case, sites with fewer neighbors exhibit a higher tendency for spin flips at low temperatures, though this effect weakens as temperature increases, leading to a higher phase transition temperature than in the planar Ising model. In the antiferromagnetic case, lattice irregularities prevent the total energy from reaching its minimum at zero temperature, highlighting the role of curvature and connectivity in shaping interactions. Phase transition temperatures are derived through specific heat, magnetic susceptibility analysis and GCN predictions, yielding  $T_c$  values for both ferromagnetic and antiferromagnetic scenarios. This work emphasizes the impact of the Fibonacci lattice's geometric properties—namely curvature and connectivity—on spin interactions in non-planar systems, with relevance to microgravity environments.

## I. INTRODUCTION

The Ising model is perhaps the simplest statistical spin model, yet it exhibits a wealth of physical phenomena and plays a crucial role across multiple fields of physics. For example, site disorder and tunable quantum fluctuations give rise to a rich variety of ground states [1–8]. The two-dimensional Ising model is among the simplest statistical models to demonstrate a phase transition. Experimentally, the Ising model can be realized using cold-atom quantum simulators [9–13]. Recently, the rapid advancement of space-based technology has driven experimental efforts to confine ultracold atoms on surfaces of various shapes in microgravity [14–24]. Among these adjustable shapes, the sphere or spherical bubble trap has garnered significant research interest, with numerous studies dedicated to exploring its geometric effects on cold atomic gases. In this paper, we focus on the Ising model confined to a spherical surface. Given the fundamental nature of the Ising model, its analysis is crucial for understanding the physical characteristics of spherical atomic gases in a microgravity environment.

The first challenge of this problem is to cover the spherical surface as uniformly as possible. Only in this way can we reliably compare the results with those of the planar square lattice. This requirement excludes the traditional latitude-longitude lattice, as the density of sites near the poles is significantly higher than anywhere else. The most suitable candidate is the Fibonacci lattice, which is essentially the most uniform spherical lattice. We have previously applied it to study the spherical XY model [25], yielding intriguing results about how vortex distribution

is significantly influenced by spherical topology. It is important to note that the Fibonacci lattice is not perfectly uniform, which complicates the analytical study of the Ising model on the Fibonacci sphere. However, by utilizing Monte Carlo (MC) simulations and machine learning techniques, we can determine the spin configurations at various temperatures and identify the phase-transition temperature of the spherical Ising model.

The second challenge arises from the irregular nature of the Fibonacci lattice, which lacks an image-like structure. Machine learning techniques have been widely used to identify phase transitions in statistical physics models, such as the Ising model. Notably, Carrasquilla and Melko [26] demonstrated the effectiveness of supervised learning with convolutional neural networks (CNNs) in classifying ordered and disordered phases in the two-dimensional square-lattice Ising model, successfully determining the critical temperature from labeled configurations. However, this approach cannot be directly applied to the Fibonacci lattice due to its non-uniform geometry. To address this, we extend the paradigm of machine learning for phase transition detection to the irregular geometry of the spherical Fibonacci lattice. Specifically, we employ graph convolutional networks (GCNs), a natural generalization of CNNs for non-Euclidean structures, which we have previously applied to study the XY model on a spherical Fibonacci lattice [25].

Recently, a study focused on the ferromagnetic Ising model on a Fibonacci-triangulated sphere found that the model exhibits a critical temperature slightly lower than that of a planar triangular lattice [27]. In this paper, we will concentrate on the mostly quadrangulated Fibonacci lattice for both ferromagnetic and antiferromagnetic Ising models, where neighbor interactions are determined by a cutoff radius  $r_c$ . Through the application of specific heat analysis and GCNs, we determined the

---

\* houxuyangwow@seu.edu.cn

† guohao.ph@seu.edu.cn

phase transition temperatures for both situations, highlighting the influence of geometric properties on spin interactions.

The rest of this paper is organized as follows: In Section II, we construct the spherical Fibonacci lattice points, ensuring that the number of lattice sites with four nearest neighbors is maximized by selecting an appropriate spin-interaction cutoff radius  $r_c$ . Sections III and IV present simulations of the spherical ferromagnetic and antiferromagnetic Ising models, respectively, using MC algorithms and GCNs. These sections include graphs illustrating spin configurations, energy, entropy and specific heat at various temperatures, as well as the phase transition temperatures for both models. Finally, Section V concludes the paper.

## II. SPHERICAL ISING MODEL

The Ising model on a 2D lattice is described by the Hamiltonian:

$$H_{\{s_i\}} = -J \sum_{\langle i,j \rangle} s_i s_j - h \sum_i s_i, \quad (1)$$

where  $s_i$  represents the spin at site  $i$ ,  $J$  is the interaction strength and  $h$  is the external magnetic field. The first summation runs over all pairs of adjacent spins, with each pair being counted only once. In this paper, we will focus on the case with  $h = 0$  for convenience. Ising models can be classified according to the sign of  $J$ : If  $J > 0$ , the interaction is called ferromagnetic; if  $J < 0$ , it is antiferromagnetic. For irregular lattices, the distance between adjacent spins may not be a constant. Therefore, it is crucial to carefully define the “nearest-neighbor sites”, which will be discussed in detail later.

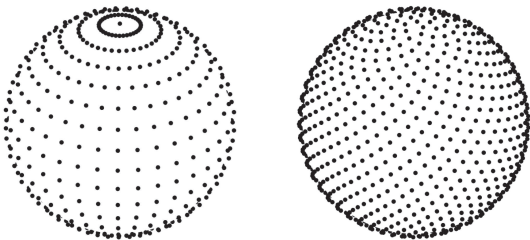


Figure 1. A comparison of the uniformity between two types of lattices of  $N = 1000$ : the latitude-longitude lattice on the left and the Fibonacci lattice on the right.

The spins of a Fibonacci Ising model are located on a Fibonacci lattice on a spherical surface. The position of each lattice site in Cartesian coordinates is given by: [28–30]

$$\begin{aligned} x_i &= \sqrt{R^2 - z_i^2} \cos(2\pi i \phi), & y_i &= \sqrt{R^2 - z_i^2} \sin(2\pi i \phi), \\ z_i &= R \left( \frac{2i - 1}{N} - 1 \right), \end{aligned} \quad (2)$$

where the notation  $i = 1, 2, \dots, N$  denotes the index of a lattice point,  $R$  represents the radius of the sphere, and  $\phi = \frac{\sqrt{5}-1}{2}$  is the golden ratio. Fig.1 compares the traditional latitude-longitude lattice with the Fibonacci lattice. Evidently, the latter is considerably more uniform than the former. Next, to compare with the properties of the Ising model on the planar square lattice, we quadrangulate the spherical Fibonacci lattice as extensively as possible. In essence, this means that the majority of spins interact with four nearest neighbors. To achieve this, we set a critical radius  $r_c$ . If the distance between two neighboring spins is less than  $r_c$ , an interaction is considered to exist between them. Firstly, we consider a system with  $N = 1000$  lattice sites as an example. To maximize the number of lattice sites with four nearest neighbors, we perform an exploratory analysis to determine the optimal nearest-neighbor radius, setting it to  $r_c = 0.1298R$ . Under these conditions, 850 spins have four neighbors, 76 spins have three neighbors, and 74 spins have five neighbors. In total, the 1000 spins collectively have 3998 neighboring connections, closely approximating the structure of a square lattice with  $N = 1000$ . We connect all “nearest-neighbor sites” and present a two perspectives of the quadrangulation of a  $N = 1000$  Fibonacci lattice from two different directions in Fig.2. Most sites appear “regular” except a few having 3 or 5 neighbors. In practical experiments, implementing a Fibonacci lattice is quite straightforward. We simply need to distribute the lattice points as evenly as possible on a spherical surface. This arrangement will naturally approximate a Fibonacci lattice in an appropriate coordinate system, as the Fibonacci lattice is fundamentally the most uniform lattice on a sphere.

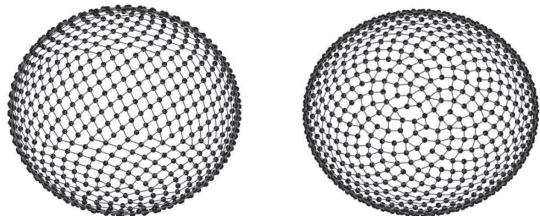


Figure 2. Perspectives of a  $N = 1000$  Fibonacci lattice from different directions.

## III. FERROMAGNETIC ISING MODEL ON A SPHERICAL FIBONACCI LATTICE

### A. Spin configurations

We first consider the case with  $J > 0$ , in which neighboring sites tend to align with the same spin orientation. This is referred to as the spherical ferromagnetic Ising model. When mapping the Ising model on a spherical Fibonacci lattice,  $r_c$  serves as a cutoff range of the interaction. We set  $J = 1$ ,  $N = 1000$  and  $r_c/R = 0.1298$ , and

use the MC techniques to obtain samples of spin configurations. We randomly flip the spins in the system and accept or reject state transitions based on the Metropolis criterion. Specifically, if the energy of the system decreases after a flip, the flip is accepted; otherwise, it is accepted only with a certain probability, known as the acceptance probability. As the temperature decreases, the acceptance probability gradually decreases and eventually reaches equilibrium.

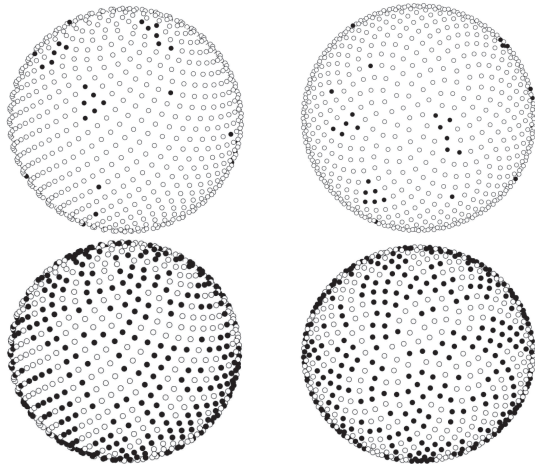


Figure 3. Spin configuration of the spherical ferromagnetic Ising Model at  $T/J = 2.0$  (Top panel) and  $T/J = 8.0$  (Bottom panel): the left panel shows the front view, while the right panel presents the top view. Up and down spins are white and black pixels.

At low temperatures, it is evident that all sites have the same spin orientation. As the temperature starts to increase, thermal fluctuations may cause spins at certain sites to reverse direction. In the top panel of Fig.3, we plot the stable spin configuration at a relatively low temperature of  $T/J = 2.0$ , where up and down spins are represented by white and black pixels, respectively. It is observed that some spins are flipped (black points), while the majority of the regions remain predominantly occupied by up spins (white points). Clearly, the system is in the ordered phase. At a very high temperature of  $T/J = 8.0$ , a significant number of spins are flipped due to thermal fluctuations. As a result, the numbers of up and down spin sites become roughly comparable. The system is now in the disordered phase, and the corresponding spin configuration is shown in the bottom panel of Fig. 3.

Note that the Fibonacci lattice is inhomogeneous, with varying probabilities of spin flips at different sites, which is crucial for understanding stable spin patterns. For instance, a site with three neighbors incurs an energy cost of  $6J$  to flip its spin, while a site with five neighbors incurs a cost of  $10J$ . Consequently, the probability of a spin-flip is relatively higher for the site with three neighbors. In the left subpanel of the top row in Fig.4, we present a view of the Fibonacci lattice from a particular

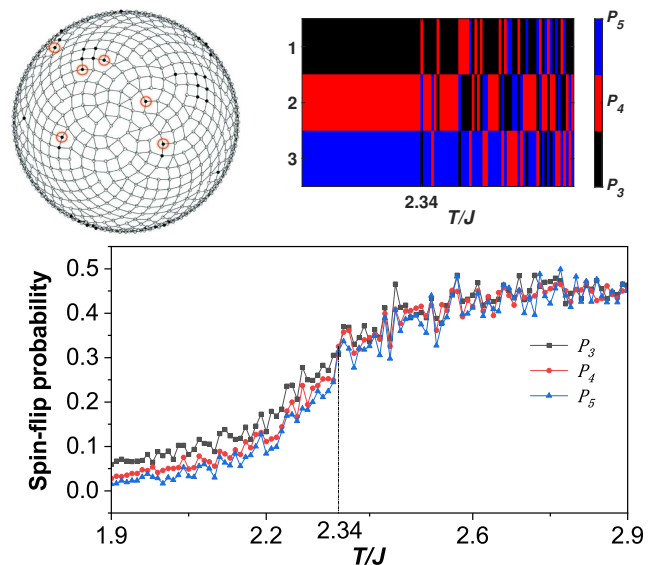


Figure 4. (Top panel) A perspective of the Fibonacci lattice at  $T/J = 2.0$ , in which the spins at 6 sites with three neighbours change direction (Left). The ranking of the statistical spin-flip probabilities  $P_3$ ,  $P_4$  and  $P_5$  at different temperatures (Right). (Bottom panel) Statistical spin-flip probabilities as functions of temperature.

direction at  $T/J = 2.0$ . It is evident that among the sites where the spin is flipped, at least 6 out of 76 sites have three neighbors. In contrast, only 11 out of 850 sites with four neighbors exhibit spin flips. This indicates that the proportion of spin flips is relatively significant for sites with three neighbors. We also statistically calculate the average spin-flip probabilities  $P_3$ ,  $P_4$  and  $P_5$  for sites with 3, 4 and 5 neighbours, respectively, across different stable spin configurations at various temperatures. The results are illustrated in the bottom panel of Fig.4, with black squares representing  $P_3$ , red disks representing  $P_4$ , and blue triangles representing  $P_5$ . To better illustrate the temperature-dependent changes in the relative spin-flip probabilities for different neighboring sites, we display the ranking of  $P_3$ ,  $P_4$  and  $P_5$  as a function of temperature in the right subpanel of the top row in Fig.4, with black, red and blue squares representing  $P_3$ ,  $P_4$ , and  $P_5$  respectively. The numbers on the left, ranging from 1 to 3, indicate the relative ranking of the values rather than their specific numerical values. Specifically, we perform ten simulations at each temperature. For each simulation, we count the number of spin flips occurring at the sites with 3, 4, and 5 neighbours in a stable spin configuration. We then compute the ratio of these flips to the total number of sites for each type to obtain the flip ratio. Finally, we average the results from the ten simulations at each temperature. At low temperatures,  $P_3 > P_4 > P_5$ , reflecting that sites with fewer neighbors are more prone to spin flips. As the temperature increases to  $T/J \gtrsim 2.34$ , thermal fluctuations become more significant relative to the energy cost of spin flips, leading to a disruption in

the ordering of  $P_3$ ,  $P_4$  and  $P_5$ . The inset of the bottom panel displays that  $P_4 > P_5 > P_3$  at  $T/J = 2.34$ . This effect has a significant impact on the phase transition temperature, as will be demonstrated later.

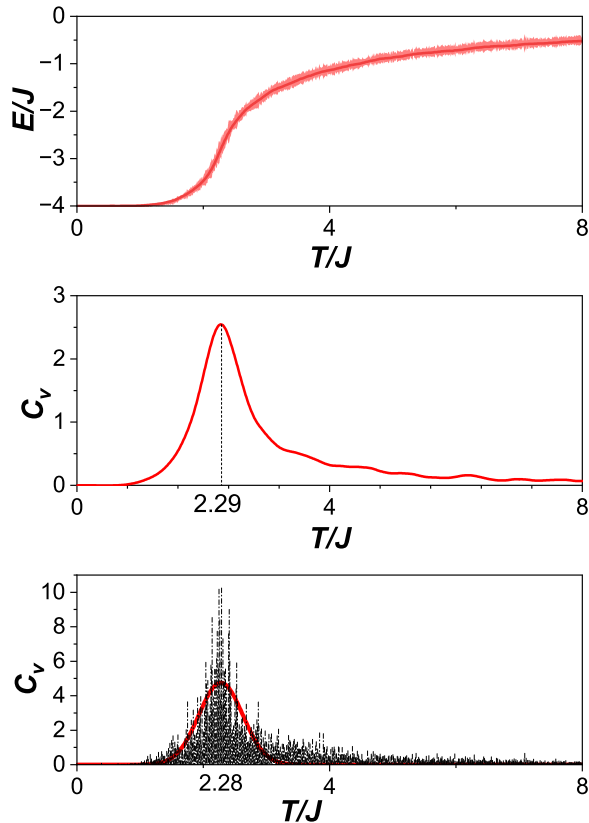


Figure 5. (Top panel) Total energy as a function of temperature for the spherical ferromagnetic Ising model with  $N = 1000$ . (Middle panel) Specific heat as a function of temperature, calculated using  $C_V = \left(\frac{\partial E}{\partial T}\right)_V$ . (Bottom panel) Specific heat as a function of temperature, calculated using Eq.(3).

### B. Determining $T_c$ via the behaviors of the specific heat and the magnetic susceptibility

Next, we aim to determine the phase transition temperature  $T_c$  of the spherical Fibonacci Ising model. To achieve this, we employ three different approaches. The first one is straightforward but relatively approximate: We estimate  $T_c$  by analyzing the behavior of the specific heat  $C_V$  using three different methods for cross-validation. The second one involves estimating  $T_c$  by analyzing the magnetization  $M$  and magnetic susceptibility  $\chi$ . The third one offers greater accuracy and involves using graph convolutional networks (GCN) to refine our estimation of  $T_c$ .

Our first method to estimate the specific heat utilizes the formula  $C_V = \left(\frac{\partial E}{\partial T}\right)_V$ . Given a stable spin configura-

tion, the total energy  $E$  of the system is calculated via Eq.(1). We then average the total energy over 10 stable spin configuration at each temperature, with a temperature interval  $0.01J$ . The numerical results are presented in the top panel of Fig.5. To estimate the specific heat, we use the spline functions to fit the  $E$  versus  $T$  curve, resulting in a function  $E(T)$ . We subsequently compute the derivative of this function to estimate  $C_V$  and plot  $C_V$  vs  $T$  in the middle panel of Fig.5. As depicted in the figure,  $C_V$  exhibits a singular behavior at  $T/J \approx 2.29$ , which can be considered as an estimate of  $T_c$ . Interestingly, this value is very close to the critical temperature of the two-dimensional Ising model on a square lattice, which is  $T_c^\square/J = 2.269$  [31]. To quantify the uncertainty in this estimation of  $T_c$ , we apply a nonparametric Bootstrap resampling approach [32, 33], which has recently been applied to the Ising model [34]. Further details of the method are provided in Appendix A. The bootstrap iteration is performed  $B = 1000$  times, yielding a more precise estimate of  $T_c$ , namely  $T_c = 2.279 \pm 0.008J$ .

The second method for estimating  $C_V$  is based on the fluctuation-dissipation formula for specific heat:

$$C_V = \frac{1}{T^2} \frac{\langle E^2 \rangle - \langle E \rangle^2}{N}, \quad (3)$$

where the Boltzmann constant is set to 1 in natural units. Here, the energy  $E$  is obtained using the previous method, and its absolute value is quite large. Therefore, when calculating  $C_V$  by using Eq.(3), the squared terms become even larger, which can significantly amplify the oscillations of  $E$ . However, the results from the previous method may be influenced by the curve fitting technique. In contrast, this method does not require calculating the slope of the fitted curve, thereby avoiding errors caused by different fitting approaches. In the bottom panel of Fig.5, we present our calculations based on Eq.(3), where each data point is averaged over 10 stable spin patterns too. As expected, the value of  $C_V$  exhibits significant oscillations as the temperature changes. However, there is also a distinct singularity around  $T \approx 2.28J$ . We further attempt to fit the curve using a Gaussian function and observe that the peak is indeed located around  $2.28J$ . To improve the accuracy of our results, we apply the Bootstrap error analysis, which refines the estimation of  $T_c$  to  $2.335 \pm 0.292J$ . Although this method introduces a larger uncertainty, the confidence interval of the results still overlaps with that obtained from the previous method.

Given the discrepancies in the values of  $T_c$  obtained from the first two methods, we consider a third method involving the entropy  $S$ , expressed as  $C_V = T \left(\frac{\partial S}{\partial T}\right)_V$ . A crucial aspect of this approach is the estimation of  $S$ . Due to the inhomogeneity of the lattice, the analytical calculation is impossible. Instead, we develop a method based on the entropy increase relative to the ground-state spin configuration. At extremely low temperatures, all sites align in the same spin state, resulting in  $S = 0$ . As the temperature increases, thermal fluctuations in-

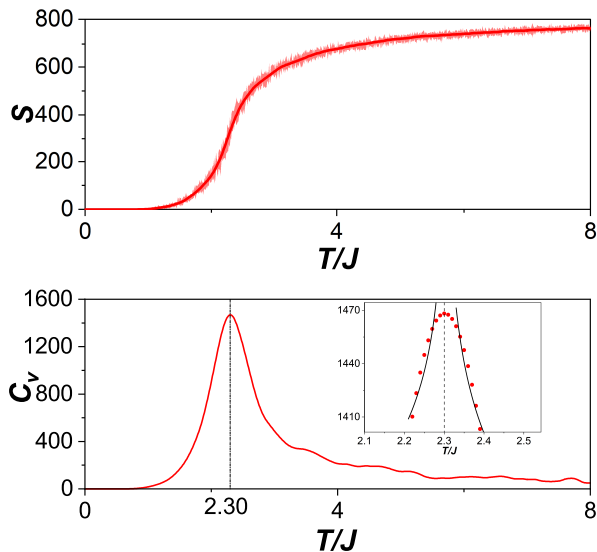


Figure 6. (Top panel) Entropy as a function of temperature for the spherical ferromagnetic Ising model with  $N = 1000$ . (Bottom panel) Specific heat as a function of temperature, calculated using  $C_V = T \left( \frac{\partial S}{\partial T} \right)_V$ . The inset shows the logarithmic fitting of data near  $T_c$ .

duce spin flips, leading to  $S > 0$ . Consequently, entropy primarily arises at the boundaries between regions with different spin orientations. The details of this method are illustrated in Appendix B. Similarly, we average over 10 stable spin configurations at each temperature, with an interval  $0.01J$ . The top panel of Fig.6 presents our estimation of  $S$  as a function of temperature  $T$ . To compute  $C_V$ , we also fit the  $S(T)$  curve using the spine functions and take its derivative. The resulting specific heat behavior is shown in the bottom panel of Fig.6. The singularity in  $C_V$  indicates that  $T/J \approx 2.30$ . Interestingly, the value of  $T_c$  obtained through this method lies exactly between the results from the first two methods. To quantify the uncertainty in the determination of  $T_c$  with this method, we employ the nonparametric Bootstrap resampling analysis again. This refinement yields  $T_c = 2.303 \pm 0.007J$ . To investigate the critical exponent of the system or the divergence of  $C_V$  near  $T_c$ , we fit the data around  $T_c$ . Among various fitting methods, the logarithmic fit,  $C_V = a - b \ln \left| 1 - \frac{T}{T_c} \right|$ , performs the best (see the inset of the bottom panel of Fig.6), suggesting that the associated critical exponent is zero. This is consistent with the 2D Ising model on a square lattice [35]. The fitted parameter  $b$  is  $47.579 \pm 7.394$  for  $T < T_c$  and  $55.103 \pm 7.281$  for  $T > T_c$ , both significantly larger than  $b = \frac{(\ln(1+\sqrt{2}))^2}{2\pi} \approx 0.1237$  for the 2D Ising model on a square lattice in the thermal dynamical limit [36]. Several factors might contribute to this discrepancy: 1. Finite-size effects: The critical exponent is defined in the limit  $N \rightarrow \infty$ . In a finite system, the maximum correlation length is constrained by the system size, modifying the details of the critical behavior.

2. Geometric effects of the spherical lattice: Unlike a planar lattice, the spherical lattice introduces structural differences that may affect critical properties. 3. Insufficient proximity to  $T_c$  (the dominant factor): Ideally, fitting should be performed around  $\Delta T/T_c \sim 0.01$ . However, for a finite system size, the singularity of the specific heat is smoothed out, limiting our study of divergence to the region around  $\Delta T/T_c \sim 0.1$ .

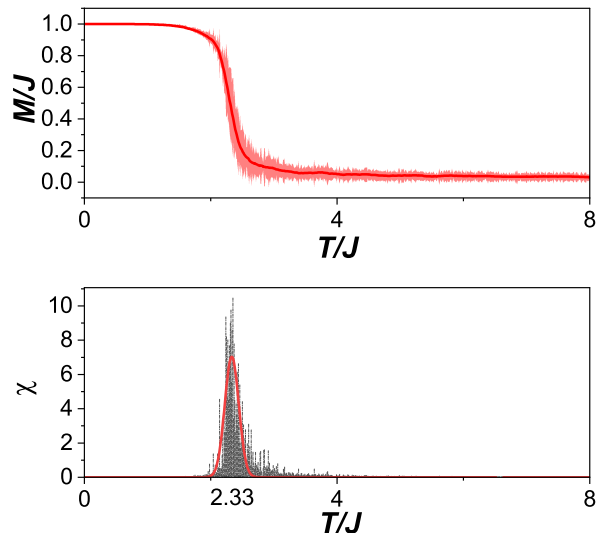


Figure 7. (Top panel) Magnetization as a function of temperature for the spherical ferromagnetic Ising model with  $N = 1000$ . (Bottom panel) Magnetic susceptibility as a function of temperature, calculated using  $\chi = \frac{\langle M^2 \rangle - \langle M \rangle^2}{NT}$ .

The phase transition temperature  $T_c$  can also be estimated by analyzing the variation of the magnetization  $M$  and magnetic susceptibility  $\chi$  with temperature. Given a stable spin configuration, the magnetization  $M$  and susceptibility  $\chi$  of the system can be calculated by

$$M = \sum_i s_i, \quad \chi = \frac{\langle M^2 \rangle - \langle M \rangle^2}{NT}. \quad (4)$$

Through methods similar to those used for analyzing the temperature dependence of energy and specific heat, we average the total magnetization and susceptibility over 10 stable spin configuration at each temperature, with a temperature interval  $0.01J$ . The numerical results are presented in Fig.7, where the top panel shows the variation of the magnetization with temperature, and the bottom panel shows the variation of the susceptibility with temperature. As depicted in the figure, the susceptibility  $\chi$  exhibits a singular behavior at  $T/J \approx 2.33$ , which can be considered as an estimate of  $T_c$ . We also apply the Bootstrap error analysis to improve the accuracy of the results, which refines the estimation of  $T_c$  to  $2.316 \pm 0.053J$ , which is close to the estimates of  $T_c$  obtained from the specific heat analysis.

### C. Determining $T_c$ via the method of machine learning

The second approach employs machine learning, which has proven to be a powerful tool in processing big data [26, 37–43]. Given that the Fibonacci lattice is not homogeneous and does not resemble a typical image-like structure, traditional CNNs can not be applied to this model [44, 45]. Instead, we utilize GCNs, which are capable of capturing spatial structural features by leveraging the connectivity relationships between nodes [46]. This makes GCNs particularly well-suited for processing topologically structured data like the Fibonacci lattice. Details of GCN implementation can be found in Appendix C.

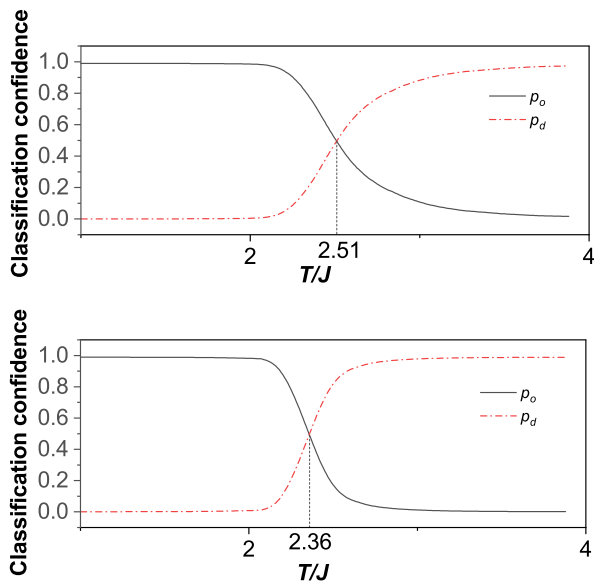


Figure 8. Classification confidences,  $p_o$  and  $p_d$ , versus temperature for the 2D Ising model on a  $20 \times 20$  square lattice (Top panel) and  $40 \times 40$  square lattice (Bottom panel).

To determine the critical temperature  $T_c$  using GCNs, we adopt a supervised learning approach inspired by prior studies [33], but tailored to our system. Unlike traditional methods that rely on training samples labeled by a classifier with prior knowledge of  $T_c$ , we take advantage of the clear separation of phases at extreme temperatures to construct our training set. Specifically, Monte Carlo (MC) spin configurations are generated at very low temperatures (e.g.,  $T/J = 0.01$ , well below the expected  $T_c$ ) and very high temperatures (e.g.,  $T/J = 8.0$ , well above the expected  $T_c$ ), where the system is unambiguously in the ordered and disordered phases, respectively. These configurations are labeled as “ordered” ( $p_o = 1$ ,  $p_d = 0$ ) and “disordered” ( $p_o = 0$ ,  $p_d = 1$ ) based on their temperature regimes, eliminating the need for an exact  $T_c$  value a priori. Here  $p_o$  and  $p_d$  represent the classification confidences for the ordered and disordered phases, respectively. The trained GCN then interpolates across

the temperature range  $[0.01, 8.0]J$ , predicting classification confidences  $p_o$  and  $p_d$  for each temperature. The intersection point where  $p_o = p_d$  is taken as the estimated  $T_c$ .

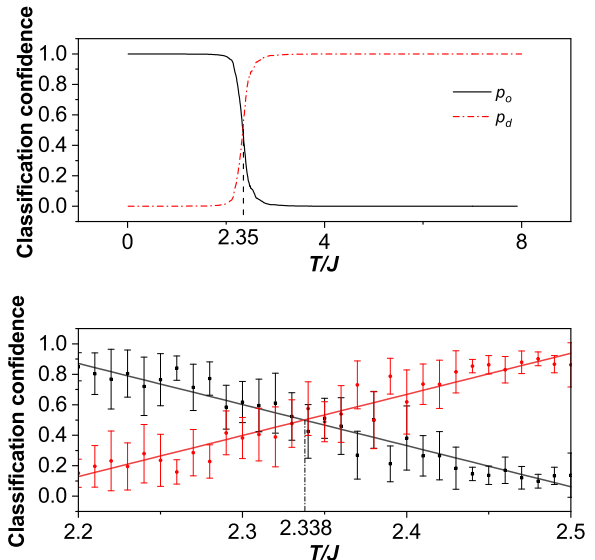


Figure 9. (Top Panel) Classification confidences,  $p_o$  and  $p_d$ , versus temperature for the ferromagnetic Ising model on a spherical Fibonacci lattice. The phase transition temperature  $T_c$  is the point at which  $p_o = p_d$ . (Bottom panel) Error analysis of  $T_c$  via linear fitting near the point  $p_o = p_d$ .

To verify the accuracy of the GCN simulations, we first investigate two-dimensional square lattices with sizes of  $20 \times 20$  and  $40 \times 40$  as a preliminary test. As illustrated in Fig.8 (with the black solid line representing  $p_o$  and the red dashed line representing  $p_d$ ), we observe that as the temperature increases, the black solid line gradually declines from 1, indicating a decreasing similarity between the simulation results and the ordered phase. In contrast, the red dashed line steadily increases from 0, reflecting an increasing similarity between the simulation results and the disordered phase. Through the simulation and analyses of different lattice scales, it is found that as the number of lattice sites increases, the phase transition temperature gradually approaches the theoretical value of  $T_c/J = 2.269$ . Specifically, the values obtained are  $T_c/J = 2.51$  for the  $20 \times 20$  lattice and  $T_c/J = 2.36$  for the  $40 \times 40$  lattice. The latter demonstrates strong concordance with the predicted critical temperature. This indicates that increasing the lattice size can enhance the accuracy of phase transition temperature estimations. Moreover, the GCN effectively captures the phase transition behavior and critical properties.

After validating the accuracy of GCN, we subsequently apply it to determine the phase transition temperature of the spherical Ising model. In numerical calculations, we select 800 temperature nodes within the range of  $[0.01, 8.0]J$ , with an interval of  $0.01J$ , and perform 100 simulations for each temperature node. The results,

presented in the top panel of Fig.9, indicate that the critical temperature is determined to be  $T_c/J = 2.35$ , where  $p_o = p_d$ . This value is fairly close to those obtained from the analysis of the specific heat  $C_V$ , but it is comparatively higher than that of the square lattice,  $T_c^\square = 2.269J$ . Due to the inhomogeneity of the Fibonacci lattice, a complete analytical analysis is not feasible. We believe a possible reason for this is the presence of sites with 3 or 5 neighbors, which affects the spin dynamics within the system. At low temperatures, a site with a greater number of neighbors is less likely to experience a spin flip, as confirmed in Fig.4. However, as the temperature increases beyond  $T \gtrsim 2.34J$ , the situation changes. Fig.4 shows that at  $T = 2.34J$ , the spin-flip probabilities follow the order  $P_4 > P_5 > P_3$  at  $T = 2.34J$ , indicating that spins on sites with 3 or 5 neighbors are more resistant to flipping. This, to some extent, enhances the “stability” of the ordered phase, effectively elevating the phase transition temperature.

To analyze the uncertainty of  $T_c$ , we note that it is determined by the intersection of the two curves  $p_o(T)$  and  $p_d(T)$ , both of which exhibit good linearity near  $T_c$ . Therefore, the uncertainty can be estimated as follows. We select an interval  $[T_1, T_2]$  around  $T_c$ , where  $p_o(T)$  and  $p_d(T)$  can be approximated as linear functions with slopes  $k_o$  and  $k_d$ , respectively. Each point on these two curves has its own uncertainty, obtained by averaging over 10 stable spin configurations. Using error propagation, we can determine the uncertainties of  $k_o$  and  $k_d$ , denoted as  $\sigma_o$  and  $\sigma_d$ , respectively. Finally, the uncertainty of  $T_c$  is given by

$$\Delta T_c = \frac{\sqrt{\sigma_o^2 + \sigma_d^2}}{|k_o - k_d|}. \quad (5)$$

In the bottom panel of Fig.9, we present our numerical results, yielding  $T_c = 2.338 \pm 0.0784J$ . Note the value  $2.338J$  is obtained from the intersection of the two linear fits, which differs slightly from  $T_c = 2.35$ , determined by the condition  $p_o = p_d$ .

#### D. Effects of $r_c$ and $N$

Now, we investigate the effects of other parameters, such as  $r_c$  and  $N$ , on  $T_c$ . First, we fix the total number of sites at  $N = 1000$  and vary the interaction length  $r_c$ . As  $r_c$  increases, each spin interacts with a greater number of spins, effectively increasing the number of neighbors per site and altering the lattice structure. In this scenario, as the temperature rises, the energy cost for a spin flip becomes larger due to the higher average number of neighbors per site, leading to an effective increase in  $T_c$ . We present our numerical results in Fig.10. The top panel shows that  $T_c = 2.35J$  for  $r_c = 0.1298R$ ,  $T_c = 3.52J$  for  $r_c = 0.1500R$ , and  $T_c = 3.95J$  for  $r_c = 0.1700R$ , which confirms our former reasoning. Moreover, the error made by GCN when performing phase classification

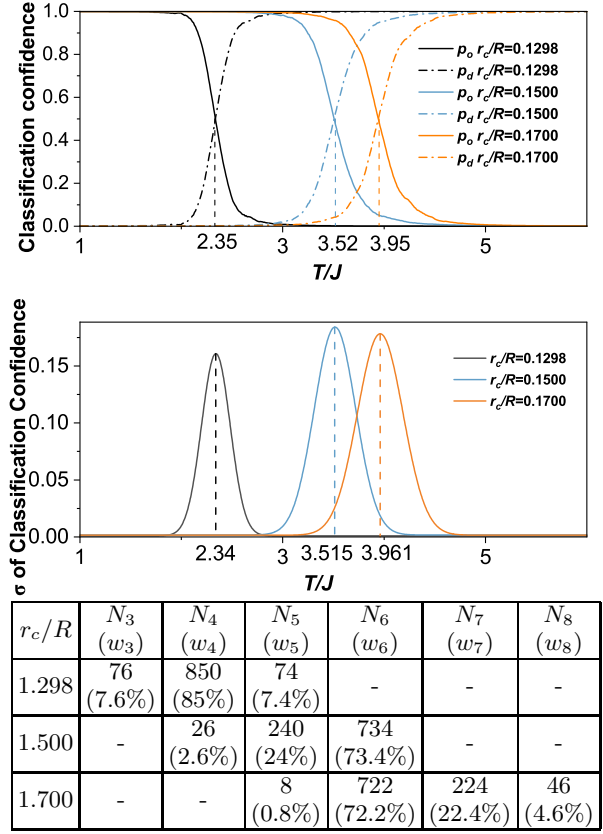
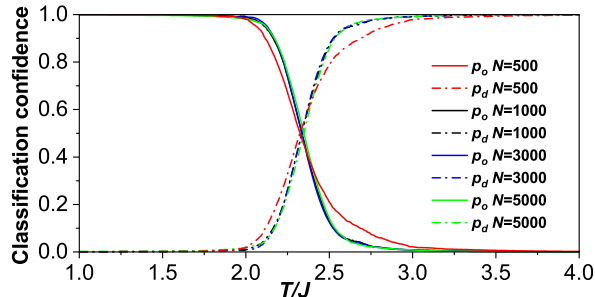


Figure 10. (Top panel) Classification confidences,  $p_o$  and  $p_d$ , versus temperature for  $N = 1000$  and different values of  $r_c$ . (Middle panel) Variances of the classification confidences as a function of temperature. (Bottom panel) Percentage of sites with different neighbors for different values of  $r_c$ . Here  $N_i$  is the number of sites with  $i$  neighbors, and  $w_i = N_i/1000$ .

can serve as an indicator for the critical behavior of a dynamical system. Consequently, the temperature at which the classification error is maximized can itself be used as a phase transition criterion [47]. To quantify this, we perform 10 independent simulations at each temperature point and compute the variance of the classification confidence. As shown in the middle panel, the maximum classification errors occur at  $T = 2.34J$  for  $r_c = 0.1298R$ ,  $T_c = 3.515J$  for  $r_c = 0.1500R$ , and  $T_c = 3.961J$  for  $r_c = 0.1700R$ , which agree well with the phase transition temperature obtained from the intersection of the two phases ( $p_o$ ,  $p_d$ ) in classification. This further supports the reliability of the maximum confusion criterion. The bottom panel lists the fraction of sites with different numbers of neighbors for various  $r_c$  values. For example, when  $r_c = 0.1500R$ , 73.4% of the sites have six neighbours, indicating that most of the lattice resembles a triangular structure. Interestingly, the estimated  $T_c = 3.52J$  is relatively close to the exact value  $T_c = 4/\ln 3 \approx 3.64J$  of the planar triangular lattice as reported in Ref.[48]. Since this model also includes some four-neighbor and five-neighbor sites, its spin flip energy

is lower than that of the six-neighbor sites, which results in a relatively lower  $T_c$ . For  $r_c = 0.1700R$ , although a similar fraction of sites have six neighbors ( $w_6 = 72.2\%$ ), the number of sites with more neighbors increases significantly ( $w_7 = 22.4\%$  and  $w_8 = 4.6\%$ ). This enhanced "neighbor interaction" effectively strengthens spin correlations, leading to a higher phase transition temperature of  $T_c = 3.92J$ .



$N$	$r_c$	$N_3 (w_3)$	$N_4 (w_4)$	$N_5 (w_5)$
500	1.8130	68 (11.6%)	418 (83.6%)	14(2.8%)
1000	1.2980	76 (7.6%)	850 (85%)	74 (7.4%)
3000	0.7470	186 (6.2%)	2740 (91.3%)	74 (2.5%)
5000	0.5818	112 (2.2%)	4740 (94.8%)	148 (3%)

Figure 11. (Top panel) Classification confidences,  $p_o$  and  $p_d$ , versus temperature for  $(N, r_c/R) = (1000, 0.1298)$ ,  $(3000, 0.747)$  and  $(5000, 0.5818)$ . (Bottom panel) Corresponding fractions of sites with different numbers of neighbors.

Next, we vary the number of lattice sites and adjust  $r_c$  accordingly to ensure the majority of sites have four neighbors. However, due to the absence of translational and rotational symmetry in the spherical Fibonacci lattice, this adjustment does not necessarily guarantee that lattices with different site numbers share similar geometric structures. This contrasts with the 2D square lattice, where structural consistency is maintained. In addition to the previously discussed case of  $N = 1000$ ,  $r_c/R = 0.1298$ , we also select  $N = 500$ ,  $r_c/R = 1.8130$ ;  $N = 3000$ ,  $r_c/R = 0.7470$  and  $N = 5000$ ,  $r_c/R = 0.5818$ , ensuring that the fractions of sites with four neighbors in the latter three cases are 83.6%, 91.3% and 94.8%, respectively. Interestingly, this suggests that the "irregular area" gradually diminishes as the effective curvature of the spherical lattice decreases. The numerical results are visualized in the top panel of Fig.11. Similarly, we determine the phase transition temperatures using two different methods mentioned before. First, by identifying the intersection of the classification confidences, we obtain  $T_c = 2.31J$ ,  $2.35J$ ,  $2.34J$  and  $2.33J$  for  $N = 500$ , 1000, 3000 and 5000, respectively. Second, using linear fitting near  $T_c$  (see the bottom panel of Fig.9), the corresponding phase transition temperatures are giving  $T_c = 2.330 \pm 0.1130J$ ,  $2.338 \pm 0.0784J$ ,  $2.336 \pm 0.0425J$  and  $2.347 \pm 0.0479J$  for the corresponding system sizes. Surprisingly, at least within the margin of error, these results do not reflect the impact of finite system size on the phase transition temperature. We hypothesize that

the following reasons may contribute to this observation: 1. Finite-size effects may not be prominent enough. Although the number of sites increases tenfold from 500 to 5000 for the same spherical surface, the interaction range  $r_c/R$  only decreases from 1.813 to 0.5818, a reduction by a factor of 3.12. More pronounced finite-size effects may require considering systems with significantly larger numbers of sites, which would demand greater computational resources. 2. The folding of the lattice onto the sphere preserves uniformity, maintaining a similarity between local and global behaviors  $N \rightarrow \infty$ . This inherent uniformity may suppress noticeable finite-size effects. All these findings suggest that even for a simple system like the Ising model, the spherical Fibonacci lattice exhibits properties distinct from those of planar lattices, similar to the observations in Ref.[27].

#### IV. ANTIFERROMAGNETIC ISING MODEL ON A SPHERICAL FIBONACCI LATTICE

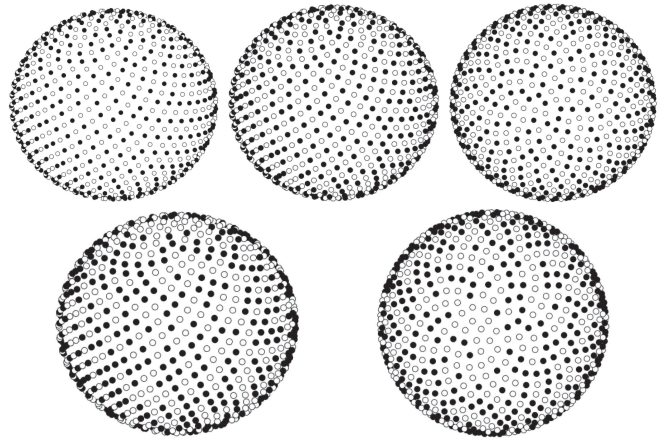


Figure 12. Top row: Spin configurations of the antiferromagnetic Ising model on a spherical Fibonacci lattice at  $T/|J| = 0.0$  (left) and at  $T/|J| = 2.0$  from two different directions (middle and right). Bottom row: Two perspectives of a stable spin configuration of the same model at  $T/|J| = 8.0$ .

We now consider the case of negative spin coupling,  $J < 0$ . In this scenario, the nearest spins tend to anti-align, leading to the formation of an ordered antiferromagnetic phase. Consequently, the connectivity features of the lattice will influence the ground-state structures. We set  $J = -1$  and focus on the spherical Fibonacci lattice with  $N = 1000$  and  $r_c/R = 0.1298$ . At zero temperature, the MC simulation predicts that most neighboring spins are oppositely aligned. However, the inhomogeneity of the spherical lattice leads to some nearest neighbors exhibiting parallel alignment. The details of the ground-state spin configuration are presented in the left panel of the top row of Fig.12. As the temperature increases, while remaining low enough, the spin distribution stays in an ordered state, though it becomes irregular at certain



sites. We present the corresponding spin configuration at  $T/|J| = 2.0$  as viewed from two different directions in the middle and right panels of the top row of Fig.12. As the temperature increases sufficiently, the ordered structure is gradually disrupted, resulting in a disordered state similar to that observed in the ferromagnetic Ising model (shown in the bottom row of Fig.3).

For 2D square lattice, the phase transition temperature of the antiferromagnetic Ising model can also be theoretically predicted,  $T_c^{\square}/J \simeq 2.269$ [31], which is the same as that of the ferromagnetic Ising model. To determine  $T_c$  for the spherical Fibonacci lattice, we will continue applying the previous methods. However, due to the less regular spin patterns and the presence of irregular neighbors on the sphere, the antiferromagnetic model exhibits exotic boundaries even at zero temperature. Therefore, the previous methods for estimating entropy and magnetic susceptibility are not applicable in this case. We can only calculate the specific heat by using  $C_V = \left(\frac{\partial E}{\partial T}\right)_V$  and Eq.(3).

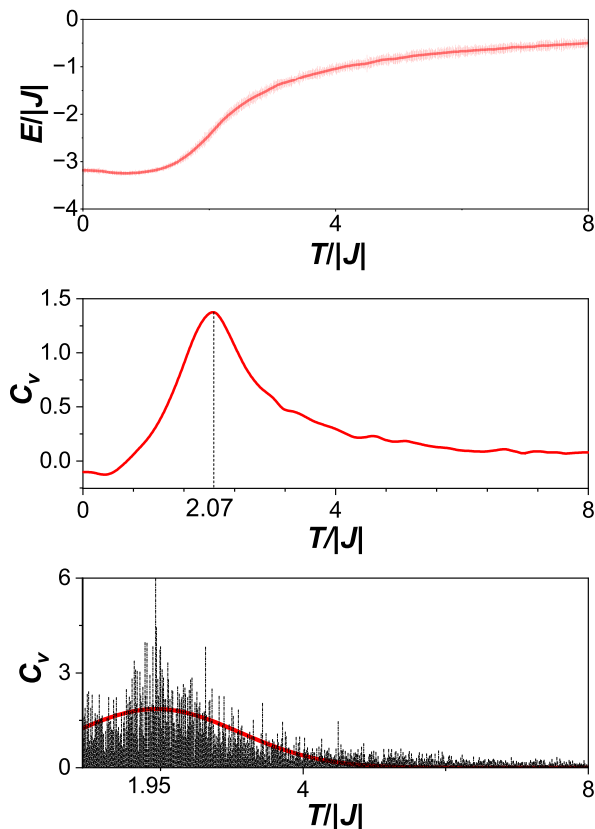


Figure 13. (Top panel) Total energy as a function of temperature for the spherical antiferromagnetic Ising model with  $N = 1000$ . (Middle panel) Specific heat as a function of temperature for the same model. (Bottom panel) Specific heat as a function of temperature, calculated using Eq.(3).

Following the same procedure, we compute the total energy for stable spin configurations at each temperature and plot  $E$  vs  $T$  in Fig.13 (top panel). By fitting

the  $E - T$  curve with spine functions and taking derivatives with respect to  $T$ , we obtain the specific heat  $C_V$ , which is also presented in Fig.13 (middle panel). Interestingly, the total energy near zero temperature is not the lowest, which contrasts with the behavior observed in the planar square lattice. This can be explained as follows. The planar square lattice is a bipartite lattice that can be divided into two sub-lattices, with sites from one sub-lattice interacting only with those from the other. If the spins on the two sub-lattices have opposite signs, the total energy is minimized. In the case of the Fibonacci lattice, the sites with 3 or 5 neighbors break this symmetry, leading to an increase in total energy, so that the most uniform spin distribution does not correspond to the lowest energy state. This is, in fact, a distinctive feature of non-uniform lattices. Furthermore, based on the behavior of  $C_V$ , we obtain an estimation of the critical temperature:  $T_c/|J| = 2.07$ , which is relatively lower than that of the ferromagnetic case. This is understandable. In an ordered phase at very low temperatures, most sites have 4 neighbors, of which 2 share the same spin. As the temperature increases, it costs  $4J$  for such a site to flip its spin, which is only half of the cost in the ferromagnetic Ising model. Consequently, the phase transition temperature is effectively lowered. After performing the Bootstrap error analysis, the result is refined to  $T_c = 2.059 \pm 0.016J$ .

To cross-check our results, we also employ Eq.(3) to analyze the behavior of  $C_V$  and present the numerical results in the bottom panel of Fig.13. Notably, the oscillations in this case are more pronounced than those in the ferromagnetic scenario. This is because the spin pattern of the ordered phase is less regular compared to the latter. In the ferromagnetic case, the ordered spin configuration is relatively simple, with most sites sharing the same spin orientation. By fitting the data with a Gaussian function, we estimate the critical temperature as  $T_c = 1.95J$ . Furthermore, Bootstrap error analysis refines this estimate to  $T_c = 1.932 \pm 0.167J$ .

Finally, we apply the method of GCN to estimate the phase transition temperature. The corresponding numerical results are visualized in the top panel of Fig.14, where the critical temperature is found to be  $T_c/|J| = 2.46$ . In the bottom panel, we present the linear fittings of  $p_o(T)$  and  $p_d(T)$  near  $T_c$ . Using Eq. (5), the estimated uncertainty is  $T_c = 2.4895 \pm 0.0610J$ . The value of  $T_c$  is fairly close to that obtained for the ferromagnetic case using the same method. This similarity may arise from the resemblance between the spin configurations of the two models at high temperatures, where both exhibit similarly chaotic spin distributions. Furthermore, the estimated  $T_c$  is also relatively higher than that derived from the behavior of  $C_V$ . This discrepancy could be due to the fact that, in the antiferromagnetic case, the distinction between the ordered and disordered phases near  $T_c$  is less pronounced than in the ferromagnetic case, which affects the GCN's ability to differentiate between the two phases. Therefore, we believe that the  $T_c$  obtained from the former

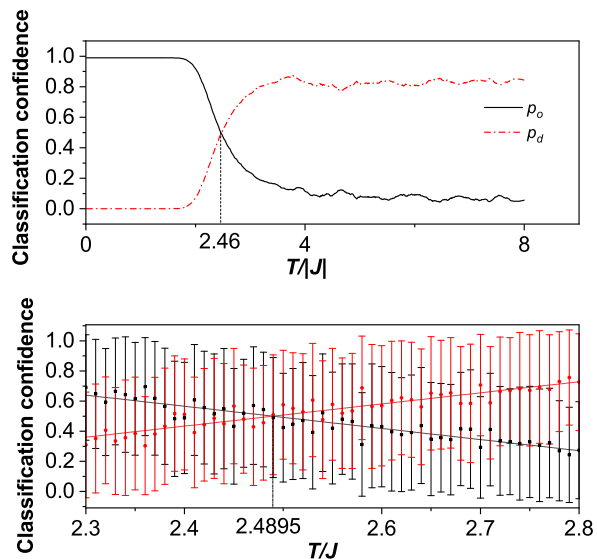


Figure 14. (Top panel) Critical temperature of the antiferromagnetic Ising model on a spherical Fibonacci lattice. (Bottom panel) The corresponding error analysis of  $T_c$  via linear fitting near the point  $p_o = p_d$ .

method is relatively more accurate. Additionally,  $p_o$  and  $p_d$  exhibit non-smooth behavior in the high-temperature regime. This irregularity arises from the inherent ambiguity in the similarity between spin configurations at low and high temperatures in the spherical antiferromagnetic Ising model, leading to suboptimal performance of the GCN in classification tasks. Nevertheless, despite these challenges, the GCN-based approach remains a valuable tool for identifying the phase transition temperature of the model.

## V. CONCLUSION

In this paper, we studied the Ising model on a spherical Fibonacci lattice, a structure that balances relative uniformity with irregular sites that significantly influence spin behavior. Employing Monte Carlo simulations and graph convolutional networks (GCNs), we analyzed spin configurations and identified phase transition temperatures for both ferromagnetic and antiferromagnetic cases.

In the ferromagnetic scenario, sites with fewer neighbors were more prone to spin flips at low temperatures, an effect that weakened as temperature rose. This behavior led to a phase transition temperature higher than that of the planar Ising model, highlighting how the lattice's curvature and connectivity bolster ferromagnetic order. Conversely, in the antiferromagnetic case, lattice irregularities prevented the total energy from reaching its minimum at zero temperature—unlike an ideal bipartite lattice—revealing the complex interplay between geometry and spin interactions in non-planar systems.

By utilizing specific heat analysis and GCNs, which

adeptly capture the lattice's geometric properties, we accurately estimated phase transition temperatures for both cases. Notably, finite size effects were minimal within the system sizes studied, likely due to the uniform distribution of sites in the spherical Fibonacci lattice, mitigating size-dependent variations common in other lattice types. These findings underscore the pivotal role of geometric features in shaping spin dynamics and phase transitions, distinguishing this system from traditional planar models.

This work enhances our understanding of the Ising model in non-planar geometries and holds particular relevance for spin systems in unique settings, such as microgravity environments, where planar assumptions may not apply. By elucidating the effects of curvature and connectivity on spin interactions, our study paves the way for future theoretical and experimental investigations into the behavior of spin systems on complex lattice structures.

## VI. ACKNOWLEDGMENTS

H.G. was supported by the Innovation Program for Quantum Science and Technology (Grant No. 2021ZD0301904) and the National Natural Science Foundation of China (Grant No. 12074064). X. Y. H. was supported by the National Natural Science Foundation of China (Grant No. 12405008) and the Jiangsu Funding Program for Excellent Postdoctoral Talent (Grant No. 2023ZB611).

### Appendix A: Bootstrap Error Analysis Method

To assess the statistical uncertainty of the estimation of  $T_c$  based on the behavior of  $C_V$ , we employ the nonparametric Bootstrap resampling method. This technique simulates statistical fluctuations in the sample distribution without assuming that the data follows a specific distribution, making it well-suited for error estimation in finite-sized systems. Using Eq.(3) as an example, the detailed steps are as follows:

#### 1. Data Preparation

Suppose the system undergoes Monte Carlo simulations at temperature points  $\{T_i\}_{i=1}^N$ . At each temperature point,  $M$  independent energy observations are collected, forming the dataset  $\mathcal{D} = \{E_{i1}, E_{i2}, \dots, E_{iM}\}_{i=1}^N$ .

$$\mathcal{D} = \{E_{i1}, E_{i2}, \dots, E_{iM}\}_{i=1}^N.$$

#### 2. Resampling Generation

For each temperature point  $T_i$ , perform random sampling with replacement:

$$\mathcal{D}_i^{(b)} = \left\{ E_{ik}^{(b)} \mid k \in \{1, 2, \dots, M\}, E_{ik}^{(b)} \sim \mathcal{D}_i \right\},$$

where the superscript  $(b)$  denotes the  $b$ -th Bootstrap iteration (with a total of  $B = 1000$  iterations).

### 3. Statistic Calculation

For each Bootstrap sample  $\mathcal{D}^{(b)}$ , compute the target statistics:

- **Specific Heat Capacity:**

$$C^{(b)}(T_i) = \frac{\langle E^2 \rangle_i^{(b)} - \langle E \rangle_i^{(b)2}}{T_i^2}.$$

- **Critical Temperature  $T_c^{(b)}$ :** Fit the  $C^{(b)}(T)$  curve with a Gaussian function and locate the peak temperature.

### 4. Error Estimation

- **Standard Deviation:**

$$\sigma_{T_c} = \sqrt{\frac{1}{B-1} \sum_{b=1}^B (T_c^{(b)} - \bar{T}_c)^2}, \quad \bar{T}_c = \frac{1}{B} \sum_{b=1}^B T_c^{(b)}.$$

- **Confidence Interval:** Take the 2.5% and 97.5% percentiles of  $\{T_c^{(b)}\}$  to define the 95% confidence interval  $[T_c^{\text{low}}, T_c^{\text{high}}]$ .

## Appendix B: Method of estimating the entropy

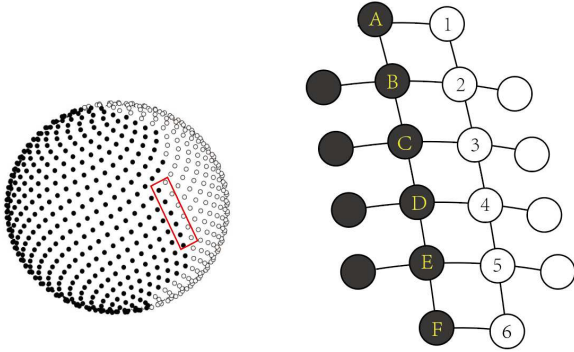


Figure 15. Boundary of a stable spin configuration and its zoom-in view.

To calculate the entropy of the spherical Ising model, we employ the Boltzmann formula:

$$S = k_B \ln \Omega, \quad (\text{B1})$$

where the Boltzmann constant is set to  $k_B = 1$  in natural unites. For a model with  $N_c$  “proper” sites at the boundaries, the total number of possible states is given by  $\Omega = 2^{N_c}$  since each spin has two orientations. This

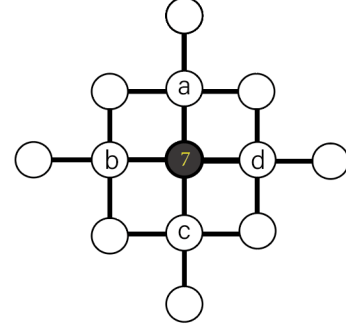


Figure 16. A special local structure of the spherical lattice.

yields  $S = N_c \ln 2$ . Thus, our primary focus is on determining the “proper” number  $N_c$  of boundary sites .

The left panel of Fig.15 presents a stable spin configuration, and a zoomed-in view of a part of its boundary is shown in the right panel. Here the boundary refers to the interface between regions of opposite spin orientations, visually represented by the white and black lattice sites. To illustrate the method for determining  $N_c$ , we select a lattice site and identify its nearest neighbor with an opposite spin. For instance, the nearest neighbor of lattice site 2 with an opposite spin is lattice site  $B$ , and so forth. However, this method results in double-counting of the boundary lattice sites, yielding  $N_c = 6 + 6 = 12$ . To correct for this, we include the lattice sites themselves in the counting process. Specifically, for lattice site 2, we record its nearest neighbor with opposite spin as site  $B$ , denoted as  $(2, B)$ . Similarly, for site 3, we record  $(3, C)$ , and so on. Likewise, for lattice site  $B$ , we record  $(B, 2)$ . Since  $(2, B)$  and  $(B, 2)$  are identical, we eliminate one duplicate entry. This refinement leads to a final determination of  $N_c = 6$ .

Now consider a more complex configuration. For instance, Fig.16 illustrates the local lattice structure of the spherical Ising model, where a single spin at site 7 is flipped downward. The boundary of this site consists of four neighboring lattice sites  $(a, b, c, d)$ . To ensure consistency with the condition for determining shown in Fig.15, we also include the lattice site itself as part of the boundary. Consequently, in this case, the “proper” number of boundary sites is 5:  $(7, a, b, c, d)$ , leading to  $N_c = 5$ .

## Appendix C: Methodology of phase classification: Details of GCN

In this paper, we use the spherical Fibonacci lattice as a sample, where the lattice information is represented as a graph  $\mathcal{G}$ . All relevant data is stored in the degree matrix  $\mathbf{D}$  and the adjacency matrix  $\mathcal{A}$ . The convolution operation is performed using the Laplacian matrix  $\mathbf{L} =$

$D - A$ .

The features of the lattice points are organized into the feature matrix  $\mathbf{X} = (\mathbf{s}_1, \dots, \mathbf{s}_N)^T \in \mathbb{R}^N$ , where  $N$  is the number of sites and  $\mathbf{s}_i$  denotes the spin at lattice site  $i$ . We then apply the Random Walk normalized Laplacian  $\mathbf{L}^{\text{rm}} = \mathbf{D}^{-1}\mathbf{L}$  for feature extraction, combining it with

the feature matrix to obtain:

$$\mathbf{H} = \text{ReLu}(\mathbf{L}^{\text{rm}}\mathbf{X}\mathbf{W}_h + \mathbf{b}_h) \quad (\text{C1})$$

Here, ReLu serves as the activation function,  $\mathbf{W}_h \in \mathbb{R}^{1 \times 1}$  is the weight, and  $\mathbf{b}_h \in \mathbb{R}^{N \times 1}$  is the bias. Finally, we employ a fully connected layer along with the *softmax* function to aggregate the hidden layer, resulting in an output  $\mathbf{H} \in \mathbb{R}^{N \times 1}$  that generates classification confidence for the ordered and disordered phases, denoted as  $p_o$  and  $p_d$ . The temperature at which  $p_o = p_d$  defines the phase transition temperature  $T_c$ .

- 
- [1] L. Onsager, *Physical Review* **65**, 117 (1944).  
 [2] C. N. Yang, *Physical Review* **85**, 808 (1952).  
 [3] M. E. Fisher, *Physical Review* **176**, 257 (1968).  
 [4] L. P. Kadanoff, *Physics Physique Fizika* **2**, 263 (1966).  
 [5] B. M. McCoy and T. T. Wu, *Physical Review* **176**, 631 (1968).  
 [6] A. B. Harris, *Journal of Physics C: Solid State Physics* **7**, 1671 (1974).  
 [7] Y. Imry and S. keng Ma, *Physical Review Letters* **35**, 1399 (1975).  
 [8] S. Sachdev, *Quantum Phase Transitions* (Cambridge University Press, 2011), 2nd ed.  
 [9] R. J. Elliott, P. Pfeuty, and C. Wood, *Phys. Rev. Lett.* **25**, 443 (1970).  
 [10] P. P. Orth, I. Stanic, and K. Le Hur, *Phys. Rev. A* **77**, 051601 (2008).  
 [11] H. Labuhn, D. Barredo, S. Ravets, S. de Léséleuc, T. Macrì, T. Lahaye, and A. Browaeys, *Nature* **534**, 667–670 (2016).  
 [12] H. Bernien, S. Schwartz, A. Keesling, H. Levine, A. Omran, H. Pichler, S. Choi, A. S. Zibrov, M. Endres, M. Greiner, et al., *NATURE* **551**, 579+ (2017).  
 [13] C. V. Parker, L.-C. Ha, and C. Chin, *NATURE PHYSICS* **9**, 769 (2013).  
 [14] N. Lundblad, R. A. Carollo, C. Lannert, M. J. Gold, X. Jiang, D. Paseltiner, N. Sergay, and D. C. Aveline, *npj Microgravity* **5**, 30 (2019).  
 [15] A. Tononi, F. Cinti, and L. Salasnich, *Phys. Rev. Lett.* **125**, 010402 (2020).  
 [16] R. Carollo, D. Aveline, B. Rhyno, S. Vishveshwara, C. Lannert, J. Murphree, E. Elliott, J. Williams, R. Thompson, and N. Lundblad, *Observation of ultracold atomic bubbles in orbital microgravity* (2021), arXiv: 2108.05880.  
 [17] A. Tononi, A. Pelster, and L. Salasnich, *Phys. Rev. Res.* **4**, 013122 (2022).  
 [18] A. Tononi, F. Cinti, and L. Salasnich, *Phys. Rev. Lett.* **125**, 010402 (2020).  
 [19] A. Tononi and L. Salasnich, *Phys. Rev. Lett.* **123**, 160403 (2019).  
 [20] N. Lundblad, R. A. Carollo, C. Lannert, M. J. Gold, X. Jiang, D. Paseltiner, N. Sergay, and D. C. Aveline, *NPJ MICROGRAVITY* **5** (2019).  
 [21] S. J. Bereta, M. A. Caracanhas, and A. L. Fetter, *Phys. Rev. A* **103**, 053306 (2021).  
 [22] T. van Zoest, N. Gaaloul, Y. Singh, H. Ahlers, W. Herr, S. T. Seidel, W. Ertmer, E. Rasel, M. Eckart, E. Kajari, et al., *Science* **328**, 1540 (2010).  
 [23] D. Becker, M. D. Lachmann, S. T. Seidel, H. Ahlers, A. N. Dinkelaker, J. Grosse, O. Hellmig, H. Muentinga, V. Schkolnik, T. Wendrich, et al., *NATURE* **562**, 391+ (2018).  
 [24] R. A. Carollo, D. C. Aveline, B. Rhyno, S. Vishveshwara, C. Lannert, J. D. Murphree, E. R. Elliott, J. R. Williams, R. J. Thompson, and N. Lundblad, *NATURE* **606**, 281+ (2022).  
 [25] C.-H. Song, Q.-C. Gao, X.-Y. Hou, X. Wang, Z. Zhou, Y. He, H. Guo, and C.-C. Chien, *Phys. Rev. Res.* **4**, 023005 (2022).  
 [26] J. Carrasquilla and R. G. Melko, *Nat. Phys.* **13**, 431 (2017).  
 [27] A. S. Pochinok, A. V. Molochkov, and M. N. Chernodub, *Ising model on the fibonacci sphere* (2023), arXiv:2301.06849.  
 [28] A. Gonzalez, *MATHEMATICAL GEOSCIENCES* **42**, 49 (2010).  
 [29] J. H. Hannay and J. F. Nye, *Journal of Physics A: Mathematical and General* **37**, 11591 (2004).  
 [30] B. Keinert, M. Innmann, M. Saenger, and M. Staminger, *ACM TRANSACTIONS ON GRAPHICS* **34** (2015), aCM SIGGRAPH Asia Conference, Kobe, JAPAN, NOV 02-05, 2015.  
 [31] M. Wadati and Y. Akutsu, in *Solitons*, edited by M. Lakshmanan (Springer Berlin Heidelberg, Berlin, Heidelberg, 1988), pp. 282–306.  
 [32] B. Efron, in *Breakthroughs in statistics: Methodology and distribution* (Springer, 1992), pp. 569–593.  
 [33] H. Kawano and T. Higuchi, *Geophysical Research Letters* **22**, 307 (1995).  
 [34] C.-Y. Lee, Ph.D. thesis (2022), URL <https://www.proquest.com/dissertations-theses/size-scaling->  
 [35] L. Onsager, *Phys. Rev.* **65**, 117 (1944), URL <https://link.aps.org/doi/10.1103/PhysRev.65.117>.  
 [36] B. M. McCoy and T. T. Wu, *The Two-Dimensional Ising Model* (Harvard University Press, 1973).  
 [37] L. Wang, *Phys. Rev. B* **94**, 195105 (2016).  
 [38] G. Carleo and M. Troyer, *Science* **355**, 602 (2017).  
 [39] K. Ch’ng, J. Carrasquilla, R. G. Melko, and E. Khatami, *Phys. Rev. X* **7**, 031038 (2017).  
 [40] D. L. Deng, X. Li, and S. DasSarma, *Phys. Rev. X* **7**, 021021 (2017).  
 [41] S. J. Wetzel, *Phys. Rev. E* **96**, 022140 (2017).  
 [42] P. Zhang, H. Shen, and H. Zhai, *Phys. Rev. Lett.* **120**, 066401 (2018).

- [43] J. Venderley, V. Khemani, and E. A. Kim, Phys. Rev. Lett. **120**, 257204 (2018).
- [44] M. J. S. Beach, A. Golubeva, and R. G. Melko, Phys. Rev. B **97**, 045207 (2018).
- [45] W. Zhang, J. Liu, and T.-C. Wei, Phys. Rev. E **99**, 032142 (2019).
- [46] J. Zhou, G. Cui, S. Hu, Z. Zhang, C. Yang, Z. Liu, L. Wang, C. Li, and M. Sun, AI Open **1**, 57 (2020).
- [47] M. N. Chernodub, H. Erbin, V. A. Goy, and A. V. Molochkov, Phys. Rev. D **102**, 054501 (2020).
- [48] R. J. Baxter, *Exactly solved models in statistical mechanics* (Elsevier, 2016).